HHS Public Access

Author manuscript

J Am Chem Soc. Author manuscript; available in PMC 2024 March 11.

Published in final edited form as:

J Am Chem Soc. 2023 August 09; 145(31): 17242–17252. doi:10.1021/jacs.3c04593.

Chiral Perovskite Nanocrystals for Asymmetric Reactions: A Highly Enantioselective Strategy for Photocatalytic Synthesis of N–C Axially Chiral Heterocycles

Kanchan Mishra,
Department of Chemistry and Biochemistry, San Diego State University, San Diego, California 92182, United States

Dylana Guyon,
Department of Chemistry and Biochemistry, San Diego State University, San Diego, California 92182, United States

Jovan San Martin,
Department of Chemistry and Biochemistry, San Diego State University, San Diego, California 92182, United States

Yong Yan
Department of Chemistry and Biochemistry, San Diego State University, San Diego, California 92182, United States;

Abstract

Catalytic approaches to generate enantiospecific chiral centers are the major premise of modern organic chemistry. Heterogeneous catalysis is responsible for the vast majority of chemical transformations, yet the direct employment of chiral solid catalysts for asymmetric synthesis is mostly overlooked. Here, we demonstrated that a heterogeneous metal-halide perovskite nanocrystal (NC) catalyst is active for asymmetric organic synthesis under visible-light activation. Chiral 1-phenylethylamine (PEA)-hybridized perovskite PEA/$CsPbBr_3$ NC photocatalysts exhibit an enantioselective (up to 99% enantiomer excess, ee) avenue to produce N–C axially chiral N-heterocycles, i.e., *N*-arylindoles from *N*-arylamine photo-oxidation. Mechanistic investigation indicated a discriminated prochiral binding of the *N*-arylamine substrates onto the chiral-NC surface with ca. −2.4 kcal/mol enantiodifferentiation. Our perovskite NC heterogeneous catalytic system not only demonstrates a promising strategy to address the long-term challenges in atroposelective pharmaceutical scaffold synthesis but also paves the road to directly employ chiral solids for asymmetric synthesis.

Corresponding Author: Yong Yan – Department of Chemistry and Biochemistry, San Diego State University, San Diego, California 92182, United States; yong.yan@sdsu.edu.

Supporting Information

The Supporting Information is available free of charge at https://pubs.acs.org/doi/10.1021/jacs.3c04593.
Experimental procedures, characterization data, NMR spectra, HPLC spectra, and GCMS traces (PDF)

The authors declare no competing financial interest.

Complete contact information is available at: https://pubs.acs.org/10.1021/jacs.3c04593

Graphical Abstract

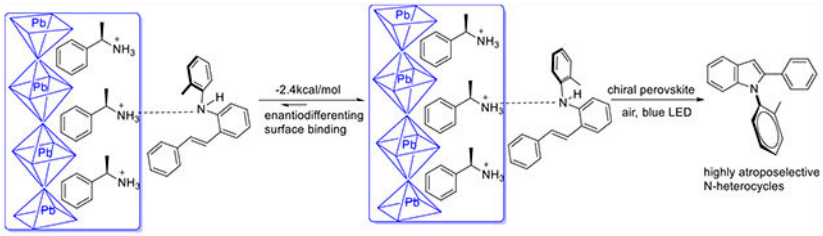

INTRODUCTION

Chirality has a profound influence on chemical, biological, and material properties.[1–6] Homogeneous asymmetric catalysis is the major approach to generate a diverse range of chiral molecules, and hence, it is the main theme of research in contemporary synthetic organic chemistry.[7–9] Heterogeneous catalytic approaches, even though they are employed to produce 90% (by volume) of the current chemical inventory,[10] yet have largely been underdeveloped with regard to asymmetric synthesis. Given the ease of product separation, simple catalyst regeneration, and usually high stability of solid catalysts facilitating continuous flow production processes, the design and development of heterogeneous asymmetric catalysts for vast and large-scale production of desirable chiral molecules should be an essential ingredient in the chemical toolbox.[11–14] In fact, ca. 50% of prescribed molecule drugs (2006–2020) brought to market are single enantiomeric chiral entities.[15] Vast and industrial-scale heterogeneous catalytic production, if achieved in an asymmetric manner, would be a potentially life-saving strategy, particularly in a global pandemic when life-saving drugs are in urgent need on a large and affordable scale.

Heterogeneous asymmetric catalysis has been reported via a combination of solid nanoparticles with a homogeneous co-catalyst, for example, cinchona-modified Pt and Pd nanomaterials for the asymmetric hydrogenation of activated C=O and C=C bonds.[16–18] The presence of homogeneous organic modifiers diminishes the significance of such strategies and does not benefit from the ease of separation and regeneration in order to facilitate a continuous process. Moreover, the structure of the enantiodifferentiating surface complex is still not well understood;[18] hence, a rational design strategy to extend such approaches to a more general class of essential chiral centers is still largely unknown and underexplored. Other successful solid asymmetric catalytic systems have also been designed,[19–25] but expensive chiral organic ligand development for homogeneous co-catalysts is still the core focus; hence, their broad application for synthetic purposes could be hindered. Recently, photoredox catalysis has provided numerous effective approaches for a myriad of synthetic organic transformations.[1,26–29] Solid-state photocatalysts have also played plausible roles in various chemical bond formations, including but not limited to C–C, C–N, C–S, C–O, and N–N bond formations.[30–33] A few examples of organic frameworks for photocatalytic asymmetric synthesis have also been reported.[34,35] The desire to design effective heterogeneous systems for broad application to address long-term challenges in enantioselective synthesis remains critical.

Enantiomer-specific N-heterocycles are extremely important in bioactive molecules, natural products, and pharmaceuticals.[36,37] Axially chiral N–C bonds are crucially significant in this category in which different atropisomers of bioactive compounds can have divergent activities,[38,39] e.g., murrastifoline F,[40] ancisheynine,[41] or hepatitis C viral polymerase inhibitors with C–N axial chirality, with only one atropisomer inhibiting the polymerase and the other being completely off-target.[39] Pharmaceutical implications of atropisomeric compounds have been largely overlooked.[36] Atropisomer chirality has a significant impact on drug development and the axial chirality should be treated as seriously as atom-centered chirality. Even though recent progress has been made,[42–45] asymmetric synthesis strategies to make the axially chiral complexes rapidly, with minimal cost, and in an efficient and selective fashion are still in a formative stage. The desire for new chemical reactions to drive the continuous evolution of organic synthesis toward atroposelective efforts is still essential.

Our research focuses on an economical and readily accessible chiral metal-halide perovskite NC photocatalyst to control the chirality of N-heterocyclization reactions, thereby developing reliable linchpin reactions that will be suitable for asymmetric drug design and development. We have previously synthesized *N*-arylpyrroles,[29] pyridazines, and pyrazolidines[46] using an efficient organic–inorganic perovskite $APbBr_3$ ($A = Cs^+$ or organic ammonium) NC photocatalyst (Scheme 1). The mechanism entails visible light-induced efficient charge transfer from the surface of perovskite NCs,[11,29,47] i.e., hole transfer from the NC to *N*-aryl amine substrates, resulting in an oxidative ring closure for N-heterocycles. Perovskite NCs also present high stability in organic solvents, fulfilling heterogeneous catalytic goals for ease of separation, regeneration, and continuous production processes. Hereby, we further question whether, when the substrates approach the catalytic surface for charge transfer, a rationally designed chiral surface of the NC may induce a prochiral substrate configuration prior to the key ring-closure step, leading to a chiral product, i.e., long-term challenging atroposelective N-heterocyclization (Scheme 1). Given that chiral metal-halide perovskites have been investigated as a way to control spin, charge, and light for applications in solar cells, spin-LEDs, chiral optoelectronics, ferroelectrics, spintronics, and so forth.[3,6,48–50] Hybrid (organic/inorganic) metal-halide perovskites also demonstrate unusually long carrier-diffusion lengths, high absorption coefficients, manageable defect states, tunable band gaps, and long spin lifetimes.[51–54] The hybrid form allows for utilizing the benefits of both the organic and inorganic properties to achieve functionality that neither the organic nor inorganic components could do by themselves. We therefore designed a hybrid perovskite with flexible tuning of the ABX_3 structures, via incorporation of the chiral organic A-site, thereby achieving chiral-NC surfaces to realize the long-challenging chiral-induced ring-closure organic reaction, i.e., N–C axially chiral atroposelective N-heterocyclization.

Here, we demonstrate that a series of hybrid organic–inorganic metal-halide chiral perovskite nanocrystals, *R*- or *S*-PEA/$CsPbBr_3$ are photocatalytically active for asymmetric organic synthesis of N–C axially chiral N-heterocycles, a critical but elusive category of atroposelective pharmaceutical scaffolds. Our catalytic methodology is able to achieve extremely high enantioselectivity, up to 99% ee, producing *N*-arylindoles with a moderate to high production yield under visible-light illumination at room temperature. Moreover, the photoredox system renders the catalytic formation of both *R*-and *S*-indole enantiomers under

R- and *S*-PEA chiral perovskites, respectively. Density functional theory (DFT) simulations indicate that the key to the high ee is the discriminated binding of prochiral *N*-arylamine substrates to the chiral-NC surface prior to the photo-induced charge-transfer process. Such discriminated substrate binding shows a significant, ca. −2.4 kcal/mol stabilized energy for the selected enantioselective pathway. Therefore, we are able to achieve a chiral surface-dictated atroposelective photocatalytic organic system.

RESULTS AND DISCUSSION

Catalyst Design and Optimization.

Due to exceptional charge-separation characteristics, metal-halide perovskite semiconductors have been previously demonstrated as catalyst candidates for photoredox reactions. Their NC forms are of particular interest; for instance, $CsPbBr_3$ NCs are stable in organic solvents and have a large surface area. As a result, such NCs have demonstrated similar levels of catalytic activity when compared to molecular catalysts, i.e., $Ir(ppy)_3$, $[Ru(bpy)_3]$, and so forth.[46] In addition to their inherent semiconductor properties, perovskite NC surfaces can also play a critical role in directing the catalytic organic reaction pathways toward desired products. Reduced dimension perovskites, i.e., those formulated with $L_2(APbBr_3)_{n-1}PbBr_4$ (L, surface organic chiral ligands), are reported with common chiral surfaces.[55–57] Colloidal perovskite NCs have also been reported with layers from $n = 1$ to $n = \infty$ by controlling the ratio of L, A, and $PbBr_2$;[55–57] particularly, their surfaces are highly tunable, i.e., chiral tune via introducing chiral-L ligands according to previous methods[4,50,58] (Figure 1). Our initiation exploration using reduced dimension chiral perovskite NCs is shown in Table 1. We found that under our organic reaction system, such reduced dimension chiral-NCs are either not forming ($n = 1$) or not stable enough ($n = 2, 3$) and are thus not desirable for the ring-closure reactions. However, NCs with reasonable stability when $n = \infty$ were synthesized by directly mixing key components via an emulsion method (**NC-1**),[58,59] (see the Supporting Information for more details), denoted as $L/APbBr_3$, particularly when L = chiral-PEA, 2-methyloctamine (2MOA), or *β*-methylphenethylamine (MPEA) replacing the surface A-site as shown in Table 1. These NCs show reactivity and lead to the desired ring-closure reaction with significant reaction yields. When changing the A-site from A = Cs to A = MA, the yield is generally lower, indicating a stable NC catalyst system with A = Cs. Overall, we found that when $n = \infty$, L = PEA, and A = Cs, the $PEA/CsPbBr_3$ leads to a good yield for N-heterocyclizations.

We then explore the enantioselectivity of this reaction using chiral-$L/CsPbBr_3$ **NC-1** to test our hypothesis, as shown in Table 1. To our delight, the reaction indeed results in an atroposelective product of *R*-**2a** when L = *R*-PEA is employed, with an ee value up to 63%, characterized via a chiral HPLC (Tables 1 and S1 in Supporting Information). When other chiral ligands were employed, i.e., *R*-MPEA, *R*-2MOA, etc., low ee (<10%) products were obtained under similar conditions. Moreover, the enantiomeric catalyst, L = *S*-PEA was also explored and led to an enantiomeric *S*-**2a**-dominated product with −56% ee. In summary, chiral perovskite NCs play a vital role in dictating the enantioselectivity of the N-heterocyclization reactions, and we found that $PEA/CsPbBr_3$ NCs exhibit both reasonable yield and ee, rendering a desirable catalytic system for this ring-closure reaction.

Chiral Surface.

With L = chiral-PEA and A = Cs, we further optimize NCs' chiral surface using various strategies to enhance the surface L-coverage because our hypothesis implies that a higher chiral surface should lead to higher enantioselectivity. We synthesized a series of *R*-PEA/$CsPbBr_3$ NCs, noted as emulsion synthesis of **NC-1**, hot injection synthesis of **NC-2**, and high-energy tip-sonication synthesis of **NC-3** using previous methods, respectively (details in the Supporting Information).[29,59–61] We assume that the surface of our NCs, i.e., surface L-sites, are either chiral-PEA or non-chiral ammonium, i.e., oleylammonium (OAm), as discussed elsewhere[4,62] (Figure 1). Chiral L-coverage is confirmed using an NMR method based upon the ratio of PEA/OAm after dissolving dry NCs in DMSO (Figure S1). As shown in Table 1, the **NC-3** shows a much higher chiral-L surface coverage. Interestingly, for **NC-3** synthesis, we find a clear phase transition (Figure S2), i.e., the high-energy tip sonication leads to a color change of NC solution during the surface ligand exchange. A completely white color intermediate is obtained during the sonication process (Figures S2 and S3), probably due to a δ-phase $CsPbBr_3$ that has been previously reported.[63] Regeneration of γ-phase cubic $CsPbBr_3$ was achieved after a prolonged high-energy sonication, as indicated by X-ray diffraction (XRD) characterization (Figure S3). However, this process leads to a significantly higher chiral-L ratio, up to 47% in **NC-3** (Table 1). In agreement with our hypothesis, the photocatalytic results show that the higher chiral-surface coverage resulted in higher enantioselectivity (Table 1). **NC-3** renders a higher than 99% ee **2a** according to our HPLC results. The reaction optimization details using **NC-3** are listed in the Supporting Information. These results demonstrate a powerful heterogeneous catalytic system for highly enantioselective N–C axially chiral organic synthesis.

The chiral-NC surface is a vital component of asymmetric catalysis, but we question if complete chiral coverage is necessary for high ee synthesis. Our NC surface ligand site is primarily occupied by OAm and the chiral ligand, but our results (Table 1) indicated that the ee value of the photocatalytic product in all the entries here is significantly higher than the chiral-L coverage. In hindsight, this is not surprising because the hole-transfer barrier from the NC to the substrates through the chiral-PEA must be drastically different from OAm. When the substrate approaches the surface for charge transfer, a long alkyl, non-conductive chain of OAm provides a significant barrier for the substrate approach and thus impedes the hole-transfer process, while aromatic PEA does not block the substrate approach, hence facilitating the charge-transfer process. Such disparity in charge transfer provides a preference for the chiral ligand-site mediating the charge-transfer over the oleylamine; therefore, a low percentage of chiral coverage, i.e., <10% of **NC-1** still results in >60% ee, while a 47% chiral surface of **NC-3** results in over 99% ee.

Chiral Catalyst Characterization.

The optimized catalyst NC-3 has been fully characterized with typical methods, i.e., scanning transmission electron microscopy(high-angle annular dark-field imaging, HAADF–STEM), UV–vis, photoluminescence (PL), and powder XRD in Figure 2a–g (see Figure S3 in the Supporting Information). All these characterizations showed no obvious difference compared with the pristine $CsPbBr_3$ NCs and indicated that the key NC properties are nearly identical to the pristine $CsPbBr_3$ with a band gap of 2.4 eV.[29,64,65] The major

difference is in the circular dichroism (CD, Figure 2h), which displays typical characteristic CD signals at 515 nm and exhibits an anisotropy factor (*g*-factor) at the NC exciton that is similar to literature reports.[4,66,67] The CD response indicates electronic coupling of the chiral ligand with the perovskite NC lattice.[4,66,67] Note that chiral-PEA ligands only show a CD response at 280 nm, far away from the NC resonance. The CD results are also corroborated with NMR studies of the surface-bound ligands, in which the dry perovskite NCs contain a high ratio of chiral-PEA occupying surface sites. Overall, the catalyst characterizations infer our proposed structure of **NC-3** PEA/$CsPbBr_3$ (Figure 1) where **NC-3**'s major semiconductor properties arise from the core $CsPbBr_3$, but the chirality arises from the surface-bound ligands.

Proposed Mechanism.

N-Arylindoles discussed above demonstrated high enantioselectivity, while the other heterocyclizations, i.e., in Scheme 1a,b, *N*-arylpyrroles or *N*-arylpyridazines showed very low or no ee with the same catalyst (see the Supporting Information). The proposed photocatalytic reaction pathway for typical N-heterocyclizations is shown in Scheme 2. Note that the generation of H_2O_2 from air is confirmed by the fluorometric hydrogen peroxide assay as reported previously.[46] We compare two perovskite-NC-induced N-heterocyclization pathways; (1) our previously developed *N*-arylpyrrole[29] formation (Scheme 2, left side with blue labels) and currently focused *N*-arylindole synthesis (Scheme 2, right side with red labels). The key feature is to illustrate the enantioselective step where the atroposelective products are generated. The pyrrole approach involves a light-induced photo-reduction of α-Br ketone, leading to the key rate-determining CH_2 radical. This radical then further reacts with *N*-arylamine to form the necessary precursor, leading to ring closure. In the pyrrole case here, this CH_2 radical does not necessarily bind to the NC surface but likely dissociates from the surface to react with free *N*-arylamine substrates. A lower ee pyrrole product is thereby expected. The key difference for the *N*-arylindole cycle is that the ring closure is occurring concurrently with the hole transfer to *N*-arylamines, enforcing a ring closure on a surface-bound prochiral substrate, **1a**. The ring-closure intermediate **1a-ring** determines the final enantioselective product because the following steps for the hydrogen-abstracted oxidation process, as proposed, do not alter the chiral center. Note that the substrate must approach the NC surface for charge transfer, probably through weak H-bonding between the *N*-arylamine substrate and the surface organic chiral L-site (1-phenylethylammonium), resulting in a high ee atroposelective *N*-arylindole.

Surface-bound chiral-PEA plays a critical role in atroposelectivity; free chiral-PEA in the reaction solution is less impactful on the final asymmetric outcome. Free PEA can dynamically form H-bonding adducts with substrate **1a**, leading to a PEA-**1a** adduct in the free solution (compared to the surface-bound adduct discussed above). However, we found that adding catalytic amounts of PEA to the reaction vessel does not lead to any meaningful enantioselectivity of **2a**. The reason is that hole transfer to the free PEA-**1a** adduct has a lower probability than direct hole transfer to the free substrate **1a**, which would not result in an enantioselective product. Note that ring closure is not required to occur in the presence of PEA if it is free in solution. As shown in Table 2, various photocatalysts, i.e., $Ru(phen)_3$ and $Ir(ppy)_3$, are able to induce the photo-oxidation and

produce the *N*-arylindoles[68–70] but result in undetectable enantioselectivity even in the presence of free chiral-PEA, similar to previous literature reports.[68] We conclude that these molecular catalysts, particularly when photoexcited, are not able to bind chiral-PEA to ensure concurrent substrate discrimination and charge-transfer-based ring closure. Even $CsPbBr_3$ NCs without sufficient surface treatment and with the presence of chiral-PEA in the solution only lead to ~15% ee. The observation of the low ee is likely due to a dynamic surface exchange of free chiral-PEA with the surface-bound OAm, forming in situ a low chiral surface coverage that then proceeds through the mechanism discussed above. Overall, the mechanism implies that concurrent substrate discrimination and charge-transfer-based ring closure are the critical steps in this photocatalytic approach for stereoinduction of high ee N-heterocycle synthesis.

DFT Simulations.

DFT simulations were employed to elucidate the key discrimination steps that result in the final enantioselectivity. Three key steps, noted as substrate surface binding, hole transfer, and ring closure, have been explored (Scheme 3). The main strategy here is to compare the energy discrepancy when a chiral surface binds to the prochiral *N*-arylamine substrate that will finally evolve into the atroposelective *R*-/*S*-products. We employed the chiral *R*-PEA as the reactive surface to weakly bind the *N*-arylamine substrates via H-bonding. The L-sites were selected according to the chiral layer of a reported crystal structure of low dimension $(R\text{-PEA})_2CsPb_2Br_7$ ($n = 2$) to mimic the chiral surface of the NCs studied here.[54,71] We also simplified the surface by freezing the structure of the chiral ligand during the calculation. Similar strategies for nanocrystal surface binding energy calculation have been explored in the literature.[72–75] The reaction pathways that lead to *R*-/*S*-products in the catalytic cycle were compared in Scheme 3. The binding energy discrepancies were explored between the chiral surface and prochiral substrate **1a**. We also compare surface binding to oxidized prochiral intermediate $\mathbf{1a}^+$ (after hole transfer). According to the reaction mechanism in Scheme 2, we assumed the chirality of **1a-ring** determines the final chirality of **2a**. Our result shows that, at the computational level of B3LYP/6–31+G in the solvent dichloromethane, with the dispersion terms including D3BJ (Grimme's third-generation dispersion and Becke–Johnson damping), a −2.4 kcal/mol binding energy of prochiral *N*-arylamine substrate *R*-**1a** is preferred when compared to its enantiomeric counterpart of prochiral-*S*-**1a** when binding to the *R*-PEA chiral surface (Scheme 3 and details in the Supporting Information). Such surface binding via a weak H-bond, N–H–N, demonstrates a ground state energy difference, implying the discrimination step may occur at the very beginning of the catalytic cycle. This binding energy difference corroborates our hypothesis that a prochiral substrate configuration forms when the substrate approaches the chiral surface for charge transfer. We further compare respective surface binding energy differences after the hole transfer, prochiral-*R*-$\mathbf{1a}^+$ (doublet state) also shows ca. −5.5 kcal/mol energy preference over the prochiral-*S*-$\mathbf{1a}^+$ intermediate (Scheme 3). Furthermore, regarding the ring-closure step, the transition state energy from prochiral-*R*-$\mathbf{1a}^+$ to ring-closure intermediate *R*-**1a-ring** is the same as that of their *S*-counterpart from *S*-$\mathbf{1a}^+$ to ring-closure intermediate *S*-**1a-ring**. We expect three such steps to govern the final enantioselectivity and the following steps in Scheme 2 may play a trivial role in determining the ee of **2a**. Here, our explorations indicate that the key discrimination step likely relies

on the initial chiral surface binding step, and the DFT simulations show that the chiral surface plays the key role in enabling enantioselectivity, i.e., binding of the prochiral-**1a** with ca. −2.4 kcal/mol energy preference or binding of oxidized *N*-arylamine intermediate prochiral-$\mathbf{1a}^{+}$ with ca. −5.5 kcal/mol favored configuration. This chiral surface-binding preference dictates the N–C axial chirality of the N-heterocycles.

Reaction Scope.

Under our reaction system, a concurrent substrate prochiral configuration and ring closure is the key to the enantioselective pathway. The previous approach for N-heterocycles in Scheme 1a for *N*-arylpyrrole likely involves a significant portion of surface-dissociated non-chiral radical intermediates, producing low ee heterocycles (see the Supporting Information). The perovskite NC-induced heterocycles in Scheme 1b require important di-radical intermediates for N–N ring closure.[29,39] It is challenging to simultaneously provoke the di-radical ring closure under a surface-induced prochiral configuration, resulting in no meaningful heterocycles under the current reaction setup. Highly enantiospecific photocatalytic N-heterocyclization has been realized for *N*-arylindole synthesis (Scheme 1c). The scope of this enantioselective photo-oxidation strategy has been revealed. A series of *N*-arylamine substrates **1a** to **1v** were prepared using the Buchwald–Hartwig amination of a 2-bromostyrene derivative with anilines. Overall, moderate to good yields of ring-closure *N*-arylindole products were produced under the optimized reaction conditions. The presence of electron-donating and electron-withdrawing groups on the aromatic rings was tolerated. Pharmaceutically important methoxy-, fluoro-, trifluoromethyl, alkyl, and nitro-substitutes are amendable using this method on indole rings. (**2a–2g**) This photocatalytic strategy also represents a general method for the regioselective introduction of substituents at the C2 and C3 positions of indoles. The CF_3, methyl, and ethyl groups at the phenyl ring of the C2 position afford a good yield (**2h–2l**). Enantioselective results are in the good to excellent range, with the ee ranging from 60 to 99% (Scheme 4). Furthermore, the scope of the N-aryl substituents has also been explored. Electron-donating groups at the para-position, i.e., methyl and methoxy-groups, are tolerant within this photocatalytic method; however, electron-withdrawing groups, i.e., the CF_3 group, gave trace amounts of product, which was identified from GCMS only (see the Supporting Information). It is interesting to point out that the ortho position was not restricted to the methyl group. The bulky *tert*-butyl group and methoxy group also give the expected products with excellent enantiomer control (**2a–2p**). Other functional group-tolerant complexes, i.e., **2q–2v**, including naphthyl and trifluoromethyl at the ortho position were also explored with successful substrates synthesized. Similarly, their respective ring-closure structures were identified using GCMS only (see the Supporting Information), but such types of complexes were in general obtained with low yields, probably due to the electron-withdrawing properties at the N-aryl position that inhibit the ring-closure reaction, similar to our previously explored N–N cyclizations in Scheme 1b.[46] The optical yields of C7-non-substituted indoles, i.e., **2e**, **2f** are generally lower than those of substituted cases, i.e., **2a, 2b**, and so forth, perhaps due to the partial racemization in former examples arising from lower rotational barriers in C7-non-substituted indoles. The typical racemization barriers of products **2a** and **2e** were determined to be 28.4 and 28.2 kcal/mol at 80 °C, respectively, and the respective half-life at room temperature is around 829 and 636 days, supporting the above results and indicating a reasonable

stable class-3 N–C axially chiral heterocycles (see the Supporting Information for more details on the racemization barriers of **2a** and **2e**). The absolute configuration of compounds **2**, estimated via HPLC and optical rotation results when compared with similar reported structures,[76,77] demonstrated a *R*-**2o** or *R*-**2a** configuration, corroborating our above DFT calculations (details in the Supporting Information).

Recycling and Regeneration.

The NC photocatalyst used in the synthesis is in the size range of 20–25 nm, as shown in Figure 2a. Centrifugation of such colloidal heterogeneous catalyst suspensions after the reaction is readily achievable; particularly, ca. 75% of the catalyst can be recovered after the reaction bath is centrifuged at 3000 rpm for 5 min, while more than 98% can be recovered at 10,000 rpm, completely different from the homogeneous catalytic approach.[76,77] The isolated and recovered catalyst demonstrated no obvious catalytic deactivation for the photo-oxidation to form N-heterocycles (see Figure S6 in the Supporting Information). However, the ee value of product **2a** decreased gradually after 4 cycles of re-use of the catalyst from 99 to 90%. The probable cause is due to a decrease in the chiral-ligand surface coverage. It is important to note that regeneration of the chiral surface can be achieved via tip sonication in the presence of free chiral-PEA ligands. Consequently, the catalyst after 4 cycles of regeneration and sonication treatment resulted in **2a** with a 99% ee, showing a fully recovered heterogeneous enantioselective approach. Such an observation is corroborated by the PXRD of the chiral perovskite NC catalyst after the recycling and regeneration experiment (see Figure S7 in the Supporting Information), showing no obvious change in the perovskite nanocrystal structure.

EXPERIMENTAL SECTION

General Procedure for Synthesis of NC-3 (Tip Sonication Method).

NC-3 was synthesized with a slight modification of the reported one.[61] First, two precursor salts, Cs_2CO_3 (33 mg, 0.1 mmol) and $PbBr_2$ (110 mg, 0.3 mmol), were taken in a dried vial and added to 10 mL of 1-octadecene. To this were added 0.5 mL of oleic acid and 0.5 mL of oleylamine. The reaction mixture was then subjected to tip sonication (FisherBrand, Fisher Scientific, FB120) for 30 min. The colorless solution gradually changed into a yellow color, exhibiting strong characteristic PL emission under UV light, indicating the formation of $CsPbBr_3$ perovskite NCs. The as-synthesized perovskite NCs were purified by centrifugation twice at a speed of 7000 rpm for 10 min to get rid of unreacted precursors. Thus, the obtained perovskite precipitates were re-dispersed in 10 mL of 1-octadecene and added to 100 μL of (*R*)-(+)-1-phenylethylamine. The yellow color of the mixture changed to white after sonication, indicating the formation of the δ-phase $CsPbBr_3$ that has been previously reported.[63] The reaction mixture was then subjected to tip sonication for a prolonged time to obtain the final **NC-3**.

General Procedure for Preparation of 2.

Chiral $CsPbBr_3$ perovskites (**NC-3**, 2 mg) were added to a solution of **1** (20 mg, 0.05 mmol) in methylene chloride/pentane (1:2) in 1 mL under air. 5 mg of SiO_2 was added to trap the molecular oxygen from the air. The mixture was stirred for 20 h under blue LEDs at

room temperature. The crude mixture was concentrated under reduced pressure and purified by flash chromatography on silica gel eluted with hexane/EtOAc = 10:0.2 to afford the corresponding product **2**.

CONCLUSIONS

Solid-state catalysts play vital roles in chemical transformations, but their impact on the production of chiral products is often overlooked. In light of recent developments of chiral metal-halide perovskites and their nanostructures, we successfully designed and cultivated a heterogeneous asymmetric catalytic system chiral-PEA/$CsPbBr_3$ to exploit the perovskite-NC properties both in highly effective photocatalysis and its structural flexibility for hybrid chirality design. The N–C axial chirality is a challenging aspect of organic synthesis but a beneficial component in pharmaceutical molecular development. Our strategy here illustrates a direct solid-state catalytic approach to produce highly valuable enantioselective N-heterocycles, paving the road to large-scale syntheses that straightforwardly benefit from separation, regeneration, and continuous process flow. The enantiodifferentiating step of the chiral perovskite NC catalysis has been clearly elucidated with a surface chiral-PEA ligand on the NC structure, where chiral discrimination occurs at the very beginning step to form a hydrogen-bonded surface prochiral-*N*-arylamine substrate. From a synthetic point of view, our approach shows that the prochiral-enantiodifferentiating mechanistic understanding is fruitful for the development of future enantioselective surface reactions, and the illustrated structure–enantioselectivity relationships would undoubtedly contribute to a rational design in order to produce a broader class of chiral centers. Chiral–phenethylamine hybridized PEA/$CsPbBr_3$ perovskite NC photocatalysts here open a new realm for a highly enantioselective strategy to produce N–C axially chiral N-heterocycles, and we expect the mechanistic structure–enantioselectivity relationships here to substantially extend the impact for solid-state asymmetric synthesis.

Supplementary Material

Refer to Web version on PubMed Central for supplementary material.

ACKNOWLEDGMENTS

The asymmetric photocatalysis was supported by the National Institute of General Medical Sciences (NIGMS), the NIH, under award R35GM147260. The development of hybrid perovskites was supported as a part of the Center for Hybrid-Organic Inorganic Semiconductors for Energy (CHOISE), an Energy Frontier Research Center funded by the Office of Science, Office of Basic Energy Sciences within the US Department of Energy.

REFERENCES

(1). Prier CK; Rankic DA; MacMillan DWC Visible Light Photoredox Catalysis with Transition Metal Complexes: Applications in Organic Synthesis. Chem. Rev 2013, 113, 5322–5363. [PubMed: 23509883]

(2). Kolb HC; VanNieuwenhze MS; Sharpless KB Catalytic Asymmetric Dihydroxylation. Chem. Rev 1994, 94, 2483–2547.

(3). Kim YH; Zhai Y; Lu H; Pan X; Xiao C; Gaulding EA; Harvey SP; Berry JJ; Vardeny ZV; Luther JM; Beard MC Chiral-induced spin selectivity enables a room-temperature spin light-emitting diode. Science 2021, 371, 1129–1133. [PubMed: 33707260]

(4). Kim Y-H; Song R; Hao J; Zhai Y; Yan L; Moot T; Palmstrom AF; Brunecky R; You W; Berry JJ; Blackburn JL; Beard MC; Blum V; Luther JM The Structural Origin of Chiroptical Properties in Perovskite Nanocrystals with Chiral Organic Ligands. Adv. Funct. Mater 2022, 32, 2200454.

(5). Lu H; Xiao C; Song R; Li T; Maughan AE; Levin A; Brunecky R; Berry JJ; Mitzi DB; Blum V; Beard MC Highly Distorted Chiral Two-Dimensional Tin Iodide Perovskites for Spin Polarized Charge Transport. J. Am. Chem. Soc 2020, 142, 13030–13040. [PubMed: 32602710]

(6). Lu H; Wang J; Xiao C; Pan X; Chen X; Brunecky R; Berry JJ; Zhu K; Beard MC; Vardeny ZV Spin-dependent charge transport through 2D chiral hybrid lead-iodide perovskites. Sci. Adv 2019, 5, No. eaay0571. [PubMed: 31840072]

(7). Genzink MJ; Kidd JB; Swords WB; Yoon TP Chiral Photocatalyst Structures in Asymmetric Photochemical Synthesis. Chem. Rev 2021, 122, 1654–1716. [PubMed: 34606251]

(8). Du J; Skubi KL; Schultz DM; Yoon TP A Dual-catalysis approach to enantioselective [2 + 2] photocycloadditions using visible light. Science 2014, 344, 392–396. [PubMed: 24763585]

(9). MacMillan DWC The advent and development of organocatalysis. Nature 2008, 455, 304–308. [PubMed: 18800128]

(10). Rothenberg G Catalysis: Concepts and Green Applications; John Wiley & Sons, 2015.

(11). Zhu X; Lin Y; Sun Y; Beard MC; Yan Y Lead-Halide Perovskites for Photocatalytic α-Alkylation of Aldehydes. J. Am. Chem. Soc 2019, 141, 733–738. [PubMed: 30602111]

(12). Heitbaum M; Glorius F; Escher I Asymmetric Heterogeneous Catalysis. Angew. Chem., Int. Ed 2006, 45, 4732–4762.

(13). Fache F; Schulz E; Tommasino ML; Lemaire M Nitrogen-Containing Ligands for Asymmetric Homogeneous and Heterogeneous Catalysis. Chem. Rev 2000, 100, 2159–2232. [PubMed: 11749286]

(14). Bartók M Unexpected Inversions in Asymmetric Reactions: Reactions with Chiral Metal Complexes, Chiral Organocatalysts, and Heterogeneous Chiral Catalysts. Chem. Rev 2010, 110, 1663–1705. [PubMed: 19873975]

(15). Nguyen LA; He H; Pham-Huy C Chiral drugs: an overview. Int. J. Biomed. Sci 2006, 2, 85–100. [PubMed: 23674971]

(16). Maeda N; Hungerbühler K; Baiker A Asymmetric hydrogenation on chirally modified Pt: Origin of hydrogen in the N-H-O interaction between cinchonidine and ketone. J. Am. Chem. Soc 2011, 133, 19567–19569. [PubMed: 22084835]

(17). Blaser H-U; Studer M Cinchona-Modified Platinum Catalysts: From Ligand Acceleration to Technical Processes. Acc. Chem. Res 2007, 40, 1348–1356. [PubMed: 17713963]

(18). Meemken F; Baiker A Recent Progress in Heterogeneous Asymmetric Hydrogenation of C=O and C=C Bonds on Supported Noble Metal Catalysts. Chem. Rev 2017, 117, 11522–11569. [PubMed: 28872309]

(19). Shaw S; White JD Asymmetric Catalysis Using Chiral Salen-Metal Complexes: Recent Advances. Chem. Rev 2019, 119, 9381–9426. [PubMed: 31184109]

(20). Zahrt AF; Athavale SV; Denmark SE Quantitative Structure-Selectivity Relationships in Enantioselective Catalysis: Past, Present, and Future. Chem. Rev 2020, 120, 1620–1689. [PubMed: 31886649]

(21). Huang Y; Hayashi T Chiral Diene Ligands in Asymmetric Catalysis. Chem. Rev 2022, 122, 14346–14404. [PubMed: 35972018]

(22). McManus HA; Guiry PJ Recent Developments in the Application of Oxazoline-Containing Ligands in Asymmetric Catalysis. Chem. Rev 2004, 35, 4151–4202.

(23). Walsh PJ; Lurain AE; Balsells J Use of Achiral and Meso Ligands to Convey Asymmetry in Enantioselective Catalysis. Chem. Rev 2003, 103, 3297–3344. [PubMed: 12914499]

(24). Leeuwen PWNMV; Kamer PCJ; Claver C; Pámies O; Diéguez M Phosphite-Containing Ligands for Asymmetric Catalysis. Chem. Rev 2011, 111, 2077–2118. [PubMed: 21087011]

(25). Mellah M; Voituriez A; Schulz E Chiral Sulfur Ligands for Asymmetric Catalysis. Chem. Rev 2007, 107, 5133–5209. [PubMed: 17944520]

(26). Romero NA; Nicewicz DA Organic photoredox catalysis. Chem. Rev 2016, 116, 10075–10166. [PubMed: 27285582]

(27). Holmberg-Douglas N; Nicewicz DA Photoredox-Catalyzed C-H Functionalization Reactions. Chem. Rev 2022, 122, 1925–2016. [PubMed: 34585909]

(28). Shaw MH; Twilton J; MacMillan DWC Photoredox Catalysis in Organic Chemistry. J. Org. Chem 2016, 81, 6898–6926. [PubMed: 27477076]

(29). Zhu X; Lin Y; San Martin J; Sun Y; Zhu D; Yan Y Lead Halide Perovskites for Photocatalytic Organic Synthesis. Nat. Commun 2019, 10, 2843. [PubMed: 31253792]

(30). Lin Y; Guo J; San Martin J; Han C; Martinez R; Yan Y Photoredox organic synthesis employing heterogeneous photo-catalysts with emphasis on halide perovskite. Chem.—Eur. J 2020, 26, 13118–13136. [PubMed: 32533611]

(31). Caputo JA; Frenette LC; Zhao N; Sowers KL; Krauss TD; Weix DJ General and Efficient C-C Bond Forming Photoredox Catalysis with Semiconductor Quantum Dots. J. Am. Chem. Soc 2017, 139, 4250–4253. [PubMed: 28282120]

(32). Vijeta A; Casadevall C; Roy S; Reisner E Visible-Light Promoted C-O Bond Formation with an Integrated Carbon Nitride-Nickel Heterogeneous Photocatalyst. Angew. Chem., Int. Ed 2021, 60, 8494.

(33). Cavedon C; Seeberger PH; Pieber B Photochemical Strategies for Carbon–Heteroatom Bond Formation. Eur. J. Org. Chem 2019, 2020, 1379–1392.

(34). Ma H-C; Chen G-J; Huang F; Dong Y-B Homochiral covalent organic framework for catalytic asymmetric synthesis of a drug intermediate. J. Am. Chem. Soc 2020, 142, 12574–12578. [PubMed: 32574049]

(35). Wu P; He C; Wang J; Peng X; Li X; An Y; Duan C Photoactive Chiral Metal–Organic Frameworks for Light-Driven Asymmetric α-Alkylation of Aldehydes. J. Am. Chem. Soc 2012, 134, 14991–14999. [PubMed: 22888952]

(36). LaPlante SR; Fader LD; Fandrick KR; Fandrick DR; Hucke O; Kemper R; Miller SPF; Edwards PJ Assessing Atropisomer Axial Chirality in Drug Discovery and Development. J. Med. Chem 2011, 54, 7005–7022. [PubMed: 21848318]

(37). Smyth JE; Butler NM; Keller PA A twist of nature – the significance of atropisomers in biological systems. Nat. Prod. Rep 2015, 32, 1562–1583. [PubMed: 26282828]

(38). Smith DE; Marquez I; Lokensgard ME; Rheingold AL; Hecht DA; Gustafson JL Exploiting Atropisomerism to Increase the Target Selectivity of Kinase Inhibitors. Angew. Chem., Int. Ed 2015, 54, 11754.

(39). LaPlante SR; Forgione P; Boucher C; Coulombe R; Gillard J; Hucke O; Jakalian A; Joly M-A; Kukolj G; Lemke C; McCollum R; Titolo S; Beaulieu PL; Stammers T Enantiomeric Atropisomers Inhibit HCV Polymerase and/or HIV Matrix: Characterizing Hindered Bond Rotations and Target Selectivity. J. Med. Chem 2014, 57, 1944–1951. [PubMed: 24024973]

(40). Bringmann G; Tasler S; Endress H; Kraus J; Messer K; Wohlfarth M; Lobin W Murrastifoline-F: First Total Synthesis, Atropo-Enantiomer Resolution, and Stereoanalysis of an Axially Chiral *N,C*-Coupled Biaryl Alkaloid. J. Am. Chem. Soc 2001, 123, 2703–2711. [PubMed: 11456955]

(41). Bringmann G; Gulder T; Reichert M; Meyer F Ancisheynine, the First N,C-Coupled Naphthylisoquinoline Alkaloid: Total Synthesis and Stereochemical Analysis. Org. Lett 2006, 8, 1037–1040. [PubMed: 16524262]

(42). Glunz PW Recent encounters with atropisomerism in drug discovery. Bioorg. Med. Chem. Lett 2018, 28, 53–60. [PubMed: 29223590]

(43). Vaidya SD; Toenjes ST; Yamamoto N; Maddox SM; Gustafson JL Catalytic Atroposelective Synthesis of *N*-Aryl Quinoid Compounds. J. Am. Chem. Soc 2020, 142, 2198–2203. [PubMed: 31944689]

(44). Kamikawa K; Kinoshita S; Furusyo M; Takemoto S; Matsuzaka H; Uemura M Stereoselective Synthesis of Both Enantiomers of *N*-Aryl Indoles with Axially Chiral N–C Bonds. J. Org. Chem 2007, 38, 3394–3402.

(45). Barrett KT; Metrano AJ; Rablen PR; Miller SJ Spontaneous transfer of chirality in an atropisomerically enriched two-axis system. Nature 2014, 509, 71–75. [PubMed: 24747399]

(46). Martin JS; Zeng X; Chen X; Miller C; Han C; Lin Y; Yamamoto N; Wang X; Yazdi S; Yan Y; Beard MC; Yan Y A Nanocrystal Catalyst Incorporating a Surface Bound Transition Metal

to Induce Photocatalytic Sequential Electron Transfer Events. J. Am. Chem. Soc 2021, 143, 11361–11369. [PubMed: 34286970]

(47). Wang K; Lu H; Zhu X; Lin Y; Beard MC; Yan Y; Chen X Ultrafast reaction mechanisms in perovskite based photocatalytic C-C coupling. ACS Energy Lett. 2020, 5, 566–571.

(48). Yu Z-G Chirality-Induced Spin–Orbit Coupling, Spin Transport, and Natural Optical Activity in Hybrid Organic–Inorganic Perovskites. J. Phys. Chem. Lett 2020, 11, 8638–8646. [PubMed: 32991181]

(49). Jana MK; Song R; Liu H; Khanal DR; Janke SM; Zhao R; Liu C; Valy Vardeny Z; Blum V; Mitzi DB Organic-to-inorganic structural chirality transfer in a 2D hybrid perovskite and impact on Rashba-Dresselhaus spin-orbit coupling. Nat. Commun 2020, 11, 4699. [PubMed: 32943625]

(50). Lu H; Vardeny ZV; Beard MC Control of light, spin and charge with chiral metal halide semiconductors. Nat. Rev. Chem 2022, 6, 470–485. [PubMed: 37117313]

(51). Quan LN; Rand BP; Friend RH; Mhaisalkar SG; Lee T-W; Sargent EH Perovskites for Next-Generation Optical Sources. Chem. Rev 2019, 119, 7444–7477. [PubMed: 31021609]

(52). Saparov B; Mitzi DB Organic-Inorganic Perovskites: Structural Versatility for Functional Materials Design. Chem. Rev 2016, 116, 4558–4596. [PubMed: 27040120]

(53). Han C; Zhu X; Martin JS; Lin Y; Spears S; Yan Y Recent Progress in Engineering Metal Halide Perovskites for Efficient Visible-Light-Driven Photocatalysis. ChemSusChem 2020, 13, 4005–4025. [PubMed: 32424894]

(54). Ahn J; Lee E; Tan J; Yang W; Kim B; Moon J A new class of chiral semiconductors: chiral-organic-molecule-incorporating organic–inorganic hybrid perovskites. Mater. Horiz 2017, 4, 851–856.

(55). Long G; Jiang C; Sabatini R; Yang Z; Wei M; Quan LN; Liang Q; Rasmita A; Askerka M; Walters G; Gong X; Xing J; Wen X; Quintero-Bermudez R; Yuan H; Xing G; Wang XR; Song D; Voznyy O; Zhang M; Hoogland S; Gao W; Xiong Q; Sargent EH Spin control in reduced-dimensional chiral perovskites. Nat. Photonics 2018, 12, 528–533.

(56). Tyagi P; Arveson SM; Tisdale WA Colloidal Organohalide Perovskite Nanoplatelets Exhibiting Quantum Confinement. J. Phys. Chem. Lett 2015, 6, 1911–1916. [PubMed: 26263268]

(57). Weidman MC; Seitz M; Stranks SD; Tisdale WA Highly Tunable Colloidal Perovskite Nanoplatelets through Variable Cation, Metal, and Halide Composition. ACS Nano 2016, 10, 7830–7839. [PubMed: 27471862]

(58). Long G; Sabatini R; Saidaminov MI; Lakhwani G; Rasmita A; Liu X; Sargent EH; Gao W Chiral-perovskite optoelectronics. Nat. Rev. Mater 2020, 5, 423–439.

(59). Huang H; Zhao F; Liu L; Zhang F; Wu X.-g.; Shi L; Zou B; Pei Q; Zhong H Emulsion Synthesis of Size-Tunable CH3NH3PbBr3 Quantum Dots: An Alternative Route toward Efficient Light-Emitting Diodes. ACS Appl. Mater. Interfaces 2015, 7, 28128–28133. [PubMed: 26652661]

(60). Protesescu L; Yakunin S; Bodnarchuk MI; Krieg F; Caputo R; Hendon CH; Yang RX; Walsh A; Kovalenko MV Nanocrystals of Cesium Lead Halide Perovskites (CsPbX3, X = Cl, Br, and I): Novel Optoelectronic Materials Showing Bright Emission with Wide Color Gamut. Nano Lett. 2015, 15, 3692–3696. [PubMed: 25633588]

(61). Tong Y; Bladt E; Aygüler MF; Manzi A; Milowska KZ; Hintermayr VA; Docampo P; Bals S; Urban AS; Polavarapu L; Feldmann J Highly Luminescent Cesium Lead Halide Perovskite Nanocrystals with Tunable Composition and Thickness by Ultra-sonication. Angew. Chem., Int. Ed 2016, 55, 13887–13892.

(62). Georgieva ZN; Bloom BP; Ghosh S; Waldeck DH Imprinting Chirality onto the Electronic States of Colloidal Perovskite Nanoplatelets. Adv. Mater 2018, 30, 1800097.

(63). Aebli M; Benin B; McCall KM; Morad V; Thöny D; Grützmacher H; Kovalenko MV White $CsPbBr_3$: Characterizing the One-Dimensional Cesium Lead Bromide Polymorph. Helv. Chim. Acta 2020, 103, No. e2000080.

(64). de Weerd C; Lin J; Gomez L; Fujiwara Y; Suenaga K; Gregorkiewicz T Hybridization of Single Nanocrystals of Cs_4PbBr_6 and $CsPbBr_3$. J. Phys. Chem. C 2017, 121, 19490–19496.

(65). Ravi VK; Markad GB; Nag A Band Edge Energies and Excitonic Transition Probabilities of Colloidal CsPbX3 (X = Cl, Br, I) Perovskite Nanocrystals. ACS Energy Lett. 2016, 1, 665–671.

(66). Kim Y-H; Zhai Y; Gaulding EA; Habisreutinger SN; Moot T; Rosales BA; Lu H; Hazarika A; Brunecky R; Wheeler LM; Berry JJ; Beard MC; Luther JM Strategies to Achieve High Circularly Polarized Luminescence from Colloidal Organic–Inorganic Hybrid Perovskite Nanocrystals. ACS Nano 2020, 14, 8816–8825. [PubMed: 32644773]

(67). Chen WJ; Zhang S; Zhou MH; Zhao TH; Qin XJ; Liu XF; Liu MH; Duan PF Two-Photon Absorption-Based Upconverted Circularly Polarized Luminescence Generated in Chiral Perovskite Nanocrystals. J. Phys. Chem. Lett 2019, 10, 3290–3295. [PubMed: 31146530]

(68). Maity S; Zheng N A Visible-Light-Mediated Oxidative C–N Bond Formation/Aromatization Cascade: Photocatalytic Preparation of N-Arylindoles. Angew. Chem., Int. Ed 2012, 51, 9562–9566.

(69). Tsuji Y; Huh KT; Watanabe Y Ruthenium-Complex-Catalyzed N-Heterocyclization. Syntheses of Quinolines and Indole Derivatives from Aminoarenes and 1,3-Propanediol of Glycols. J. Org. Chem 1987, 52, 1673–1680.

(70). Jouffroy M; Primer DN; Molander GA Base-Free Photoredox/Nickel Dual-Catalytic Cross-Coupling of Ammonium Alkylsilicates. J. Am. Chem. Soc 2016, 138, 475–478. [PubMed: 26704168]

(71). Fiuza-Maneiro N; Sun K; López-Fernández I; Gómez-Graña S; Müller-Buschbaum P; Polavarapu L Ligand Chemistry of Inorganic Lead Halide Perovskite Nanocrystals. ACS Energy Lett. 2023, 8, 1152–1191.

(72). Lin Y; Avvacumova M; Zhao R; Chen X; Beard MC; Yan Y Triplet Energy Transfer from Lead Halide Perovskite for Highly Selective Photocatalytic 2 + 2 Cycloaddition. ACS Appl. Mater. Interfaces 2022, 14, 25357–25365. [PubMed: 35609341]

(73). Bodnarchuk MI; Boehme SC; ten Brinck S; Bernasconi C; Shynkarenko Y; Krieg F; Widmer R; Aeschlimann B; Günther D; Kovalenko MV; Infante I Rationalizing and Controlling the Surface Structure and Electronic Passivation of Cesium Lead Halide Nanocrystals. ACS Energy Lett. 2019, 4, 63–74. [PubMed: 30662955]

(74). Goesten MG; Hoffmann R Mirrors of Bonding in Metal Halide Perovskites. J. Am. Chem. Soc 2018, 140, 12996–13010. [PubMed: 30207152]

(75). Jiang Y; Weiss EA Colloidal Quantum Dots as Photo-catalysts for Triplet Excited State Reactions of Organic Molecules. J. Am. Chem. Soc 2020, 142, 15219–15229. [PubMed: 32810396]

(76). Kitagawa O Chiral Pd-Catalyzed Enantioselective Syntheses of Various N–C Axially Chiral Compounds and Their Synthetic Applications. Acc. Chem. Res 2021, 54, 719–730. [PubMed: 33481580]

(77). Ototake N; Morimoto Y; Mokuya A; Fukaya H; Shida Y; Kitagawa O Catalytic Enantioselective Synthesis of Atropisomeric Indoles with an N–C Chiral Axis. Chem.—Eur. J 2010, 16, 6752–6755. [PubMed: 20461829]

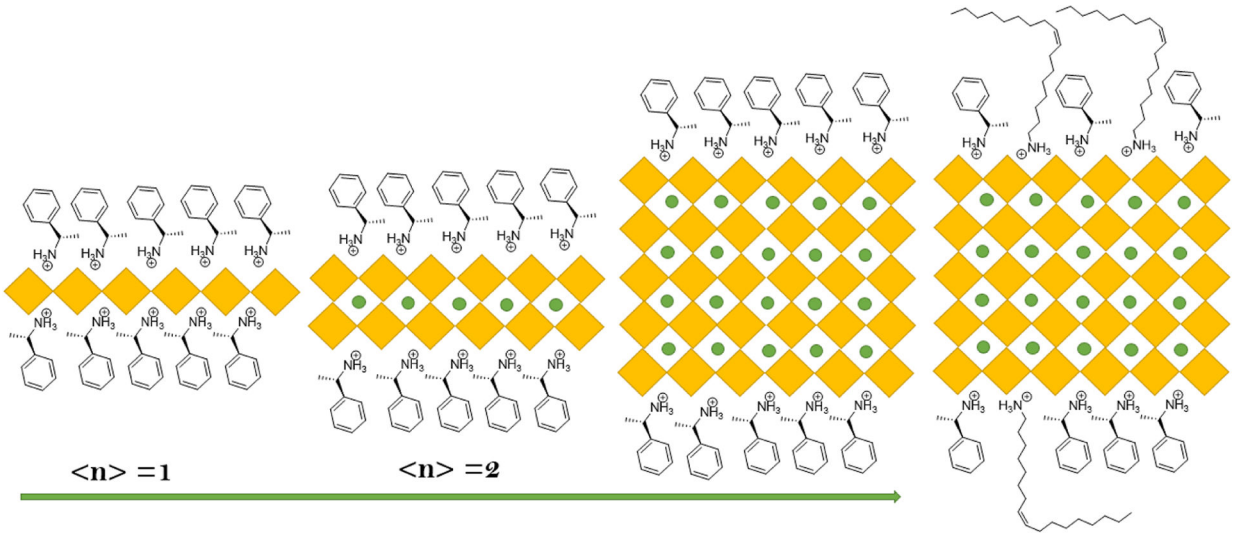

Figure 1.

Chiral perovskite NCs. NCs formulated with $L_2(APbBr_3)_{n-1}PbBr_4$. Right: proposed structure of NC-3 ($n = \infty$).

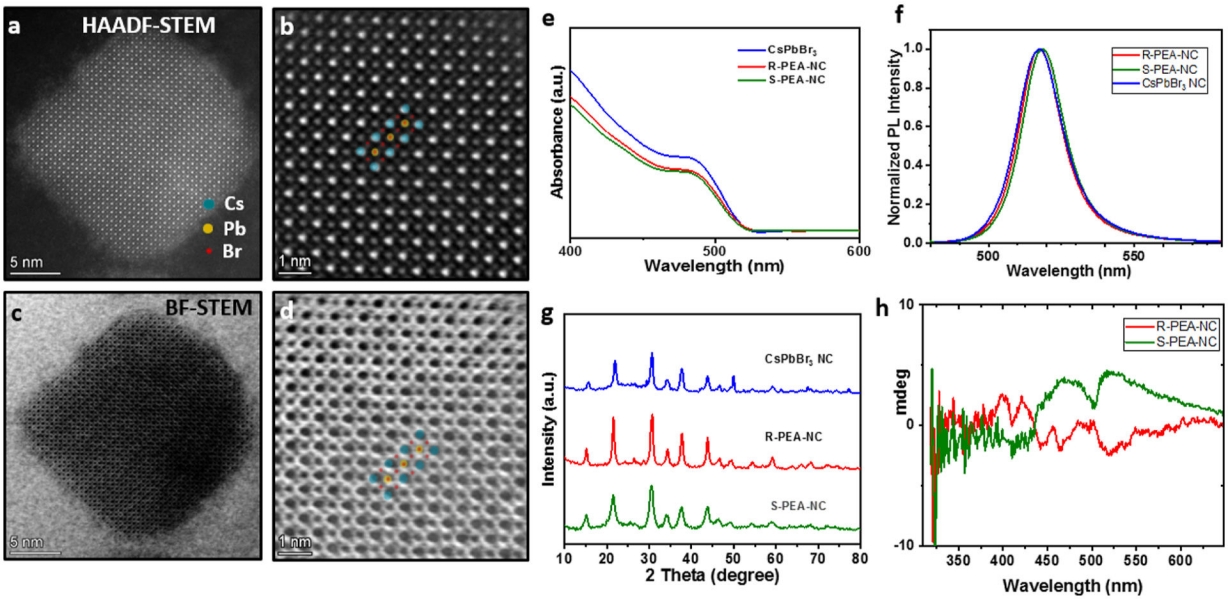

Figure 2.

NC-3. (a–d) STEM; (e) UV–visible spectra of $CsPbBr_3$, *R*-NC-3, and *S*-NC-3, (f) PL, (g) PXRD, and (h) CD spectra of *R*-NC-3 and *S*-NC-3.

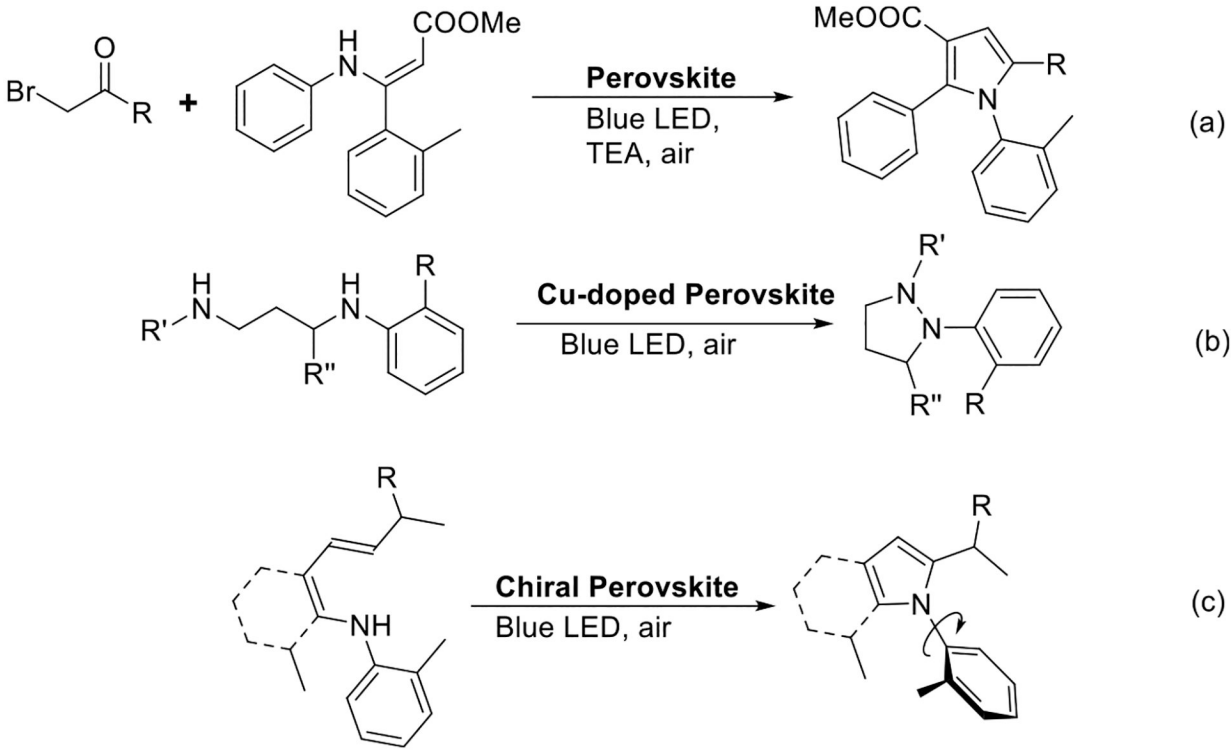

Scheme 1.

Perovskite for Photocatalytic N-Heterocycle Synthesis: (a,b) Previous Examples with Potential Atroposelective Approaches; (c) This Work

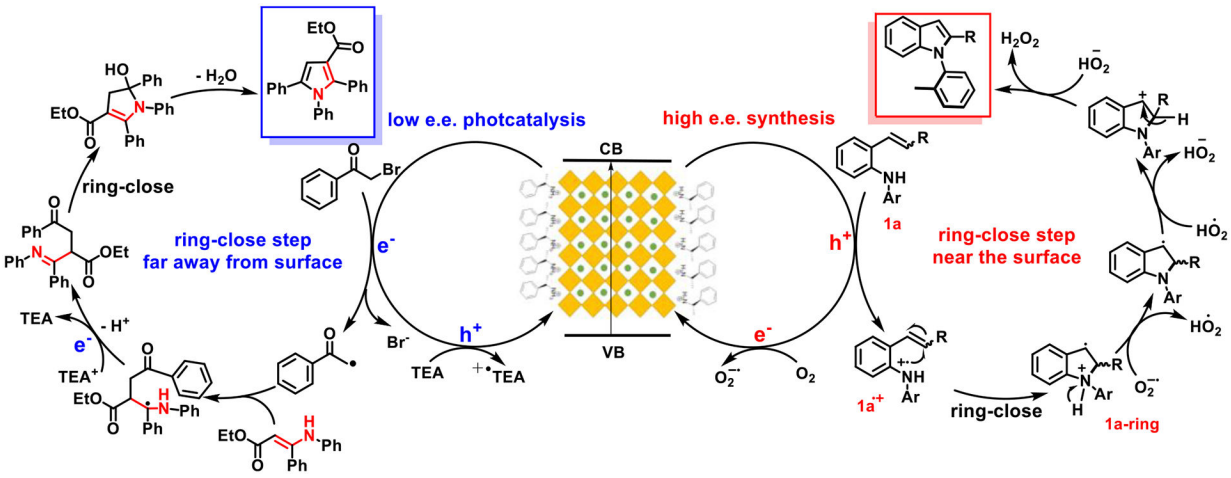

Scheme 2.

Proposed Mechanism for (a) *N*-Arylpyrrole and (b) *N*-Arylindole

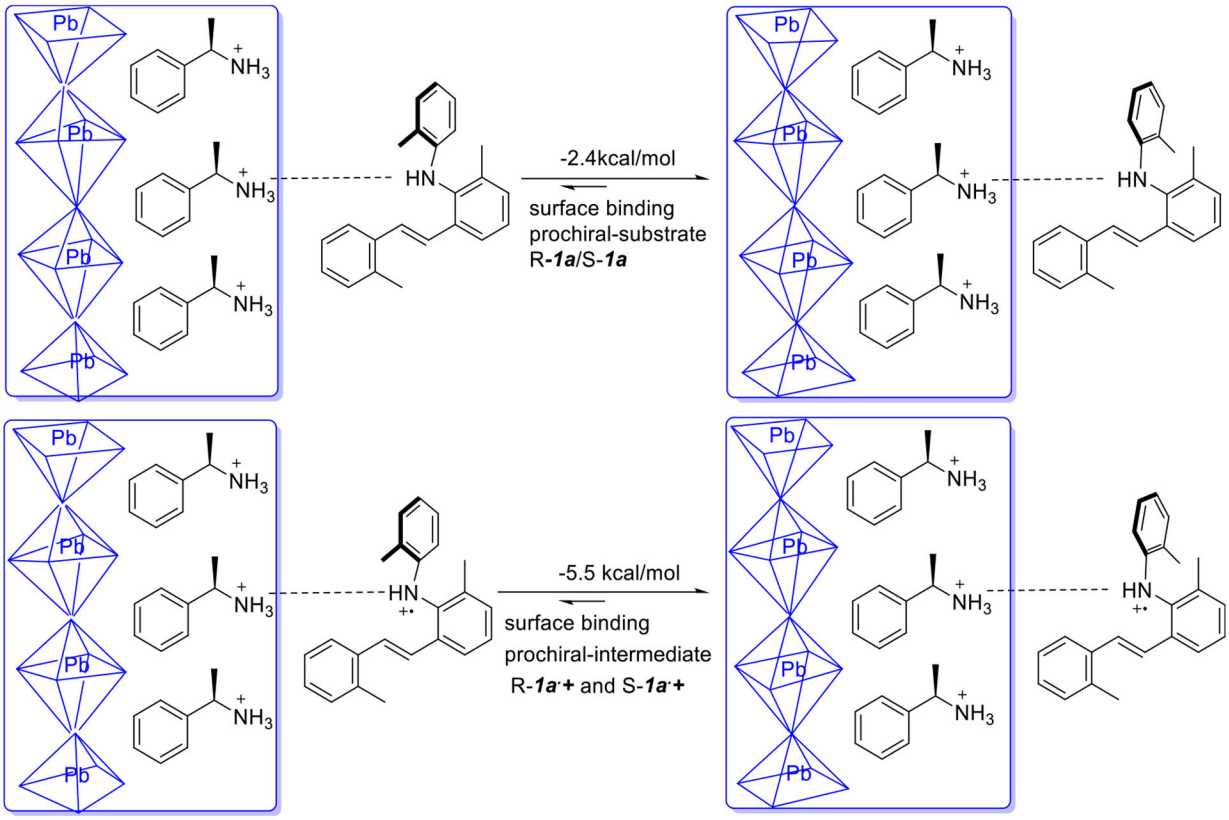

Scheme 3.

DFT Studies; Binding Energy Discrepancies between the Chiral Surface and 1a (Up), $1a^{+}$ (after Hole Transfer)

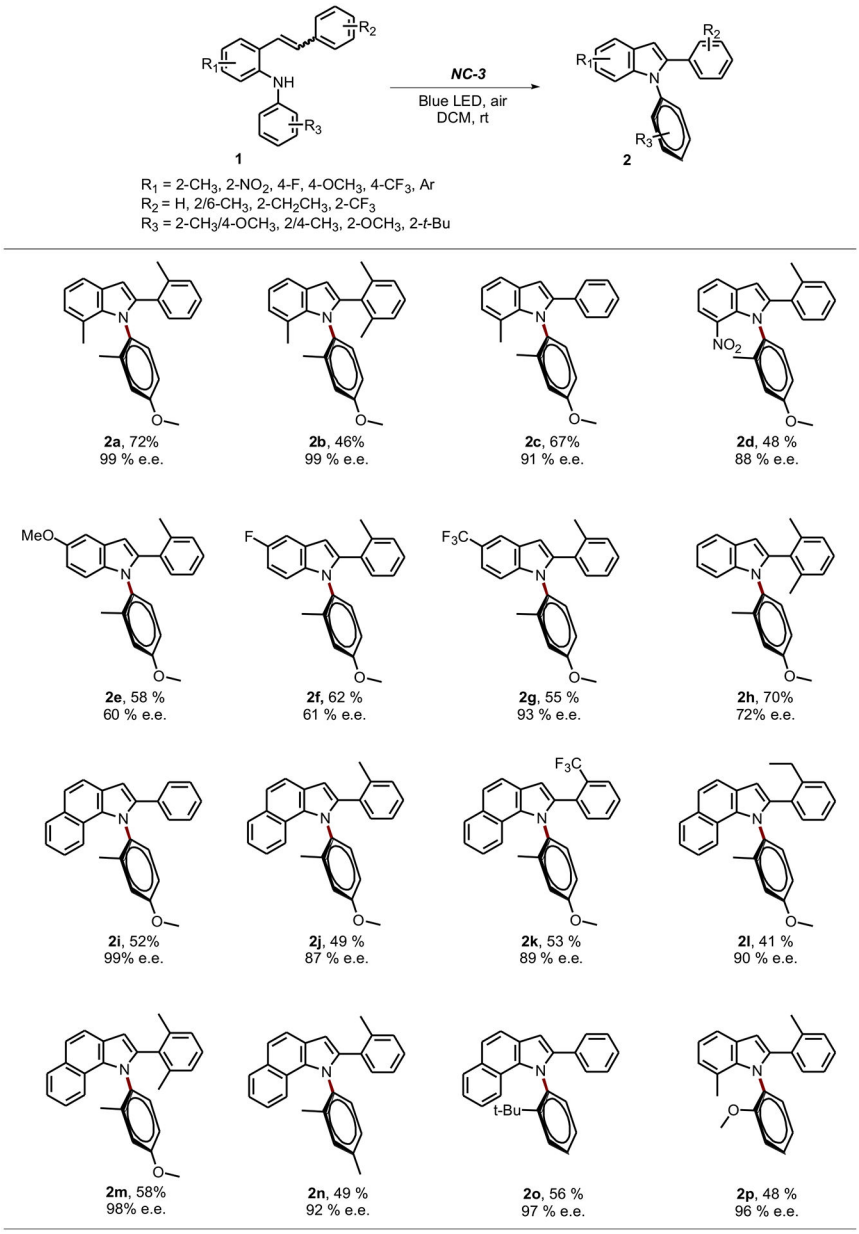

Scheme 4.

Reaction Scope: Conditions: NC-3 (2 mg), CH_2Cl_2/Pentane, SiO_2, Air, and Blue LED at Room Temperature. ee % via Chiral HPLC

J Am Chem Soc. Author manuscript; available in PMC 2024 March 11.

Table 1.

Catalyst Design and Optimization

NC-1: $L_2(APbBr_3)_{n-1}PbBr_4$			perovskite formation[a]	stability in CH_2Cl_2[b]	2a, % yield[c]	ee, %[d]
$n = 1$	L = *R*-PEA		no			
$n = 2$	L = *R*-PEA	A = Cs	yes	no	0	
	L = *R*-PEA	A = MA	yes	no	0	
	L = *R*-2MOA	A = Cs	yes	no	0	
$n = 3$	L = *R*-PEA	A = Cs	yes	no	0	
	L = *R*-2MOA	A = Cs	yes	no	0	
$n = \infty$	L = *R*-PEA	A = MA	yes	yes	16	
	L = *R*-PEA	A = Cs	yes	yes	51	63
	L = *R*-2MOA	A = Cs	yes	yes	72	<10
	L = *R*-2MOA	A = MA	yes	yes	28	n.d.
	L = *R*-MPEA	A = Cs	yes	yes	45	<10
	L = *S*-PEA	A = Cs	yes	yes	50	−56
$PEA/CsPbBr_3$			**ratio of PEA/OAm**	**estimated L coverage, %**		**ee, %**

NC-1 (emulsion)	0.1	9	63
NC-2 (hot injection)	0.2	17	83
NC-3 (tip sonication)	0.9	47	99

[a] $n = 1$, no NCs formed in our system; $n > 1$, via characteristic perovskite absorption.

[b] Via characteristic perovskite absorption, $n = 2$ or 3 perovskite absorption disappeared immediately in normal organic solvents, i.e., CH_2Cl_2.

[c] Reaction conditions: **1a** (0.05 mmol), open to air, in CH_2Cl_2 solvent, irradiation with 456 nm Kessil blue LED at room temperature, isolated yield reported here.

[d] Determined by HPLC analysis. n.d. = not detected.

Table 2.

Photocatalyst Comparisons for Enantioselective Synthesis of 2a

entry	photocatalyst	co-catalyst (10 mol %)	yield %[a]	ee %[b]
1	$Ru(phen)_3$	*R*-PEA	68	n.d.
2	$Ir(ppy)_3$	*R*-PEA	87	n.d.
3	$CsPbBr_3$	*R*-PEA	79	~15
4	**NC-3**		72	>99

[a]Reaction conditions: **1a** (0.05 mmol), SiO_2, open to air, irradiation with Kessil 456 nm LED at room temperature, isolated yield.

[b]Determined by HPLC analysis.